RSC Advances




ROYAL SOCIETY OF CHEMISTRY

www.rsc.org/advances

*Graphical abstract of*

# Non-thermal plasma treated gold catalyst for CO oxidation

Huiyuan XU, Jingjie LUO,* Wei CHU*

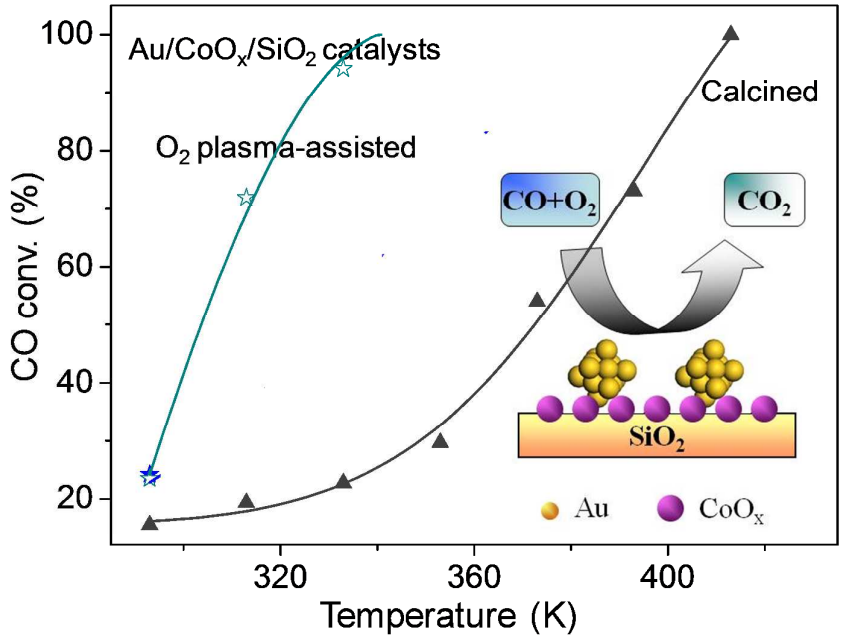


Plasma under oxygen atmosphere is available for promoting the microporosity, the redox property, and the catalytic performance of gold nanoparticles.

RSC Advances

RSCPublishing

ARTICLE

# Non-thermal plasma treated gold catalyst for CO oxidation

Cite this: DOI: 10.1039/xoxxoooooox

Huiyuan XU,[a,b] Jingjie LUO,*[b,c] Wei CHU*[b]

Received ooth January 2012,
Accepted ooth January 2012

DOI: 10.1039/xoxxoooooox

www.rsc.org/

Abstract The $CoO_x$ doped silica and its supported gold nanoparticles were synthesized by conventional thermal treatment or plasma treatment. The activity for CO oxidation displayed 100% CO conversion at only 338 K over the $O_2$ plasma-treated $Au/CoO_x/SiO_2$-PO. The analyzing results suggested that, different from the traditional calcined gold catalyst, the metal particles in the plasma-treated samples tended to be smaller and homogeneous and highly dispersed on the surface of support. The microstructure such as large surface contact and the mesoporosity were more appropriate for the reactions. In addition, the $O_2$ atmosphere plasma treated samples obtained large amount of oxygen supply center, which in turn facilitated the proceeding of low-temperature CO oxidation. Plasma technique under oxygen atmosphere, was proved as an efficient treatment technique for gold catalysts.

## 1. Introduction

Plasma is one of the four fundamental states of subjects except the liquid, gas, and solid. It is a kind of gas consisted with charged particles. The ionization can be accomplished by means of many methods such as exposing gases under electronic filed.[1, 2] During the past several decades, plasmas were applied for the treatment of materials in physics, chemistry, and biology fields.[3, 4] The non-thermal plasmas usually possess low temperature, non-thermodynamic equilibrium, and low pressure,[5] which is capable to resist the structure and crystal form destruction resulted from the high temperature. In the catalysis field, the corresponding thermal effects and chemical reactions may help to enhance the active sites-support interaction and facilitate the particle dispersion.[6-8] The related researches of plasma impacting the structure, the performance, and the morphologies of materials demonstrated that the plasma technique should act as an efficient treatment for pretreating or synthesizing novel and useful materials.[9-11]

Supported gold nanoparticles for a long time have been considered as one of the most efficient catalysts for CO oxidation. The attention paid on new catalysts related to gold materials is continuously incremental. The investigations on gold nanoparticles supported on silica were commonly reported in literatures although such material general performed unsatisfied activity, focusing on the understanding of reaction mechanism or seeking solutions for enhancing catalytic activity. On the other hand, the investigations such as impacts of different supports or additional active elements,[12-14] the special treatments and synthesis techniques also become the prevalent solutions for purchasing high efficiency gold catalysts with great low-temperature activity with minimum energy and material costs.[15, 16] However, as far as we know, the intersection between gold catalysts and non-thermal glow discharge plasma technique is still in minority. How the plasma technique impacts the gold-concerning materials and the possible performance for reactions such as CO oxidation still needs detailed supplementation.

In this work, the influence of plasma treatment on the properties and performances of $CoO_x/SiO_2$ and its supported gold nanoparticles were synthesized. The low-temperature CO oxidation was applied as probe. Combining the results from $O_2$-TPD, $N_2$ adsorption-desorption, FT-IR, SEM, XRD, TEM, and XPS techniques, the impacts of plasma treatment on the morphology, structure, size distribution and reducibility of gold nanoparticles were discussed in detail.

## 2. Experimental

### 2.1 Materials

The silica (Qingdao Haiyang Chemical Co., Ltd) modified with $CoO_x$ (6 wt% $Co/SiO_2$ molar ratio) by isometric impregnation method. The obtained sample powder was divided into two portions. The first portion was calcined under air at 533 K for 4 h, denoted as $CoO_x/SiO_2$-C. The chosen of calcination temperature was based on the results of thermal gravimetric analysis. The other portion was posed in the quartz tube and further went through plasma treatments under $O_2$ atmosphere without further calcination, respectively. The obtained sample was labeled as $CoO_x/SiO_2$-PO. The $HAuCl_4$

was applied as gold precursor and supported on to the $CoO_x/SiO_2$ material (before calcination) by deposition-precipitation method. The $HAuCl_4 \cdot 4H_2O$ (Sinopharm Chemical Reagent Co. Ltd; Au content 47.8%) was utilized as the gold precursor. The $HAuCl_4 \cdot 4H_2O$ aqueous solution and the precipitation agent-ammonia were slowly co-added into a three-necked bottle containing $CoO_x/SiO_2$ at room temperature, with the pH value controlled between 8 and 9. The sample was stirred for 4 h, then filtered and washed for several times. The resulting powder was dried at 333 K for 24 h. The corresponding material was also divided into two portions: the first portion was calcined in air at 473 K for 4 h; the other portion was treated by plasmas under $O_2$ without further calcination, respectively, and named as $Au/CoO_x/SiO_2$-PO. We also made the $Au/SiO_2$-C sample by the same DP method as reference. The theoretical value of gold loading was 1.5 wt%. The mass content of gold detected by ICP-AES in $Au/CoO_x/SiO_2$-C and $Au/CoO_x/SiO_2$-PO catalysts was 1.48% and 1.50%, respectively.

### 2.2 Plasma treatment

The thermal plasma treatments of samples were processed under the GP 062DL3 type capacitive coupled high-frequency plasma generator (provided by Chengdu Institute of Organic Chemistry of Chinese Academy of Science). The air pressure was fixed at 40 Pa, and the radio frequency was 1312 MHz with 100 V voltage. The anode current and grid current were 90 mA, and 30 mA, respectively. The catalyst precursors were treated under $O_2$ for 45 min. The above description was also added in the experimental part.

### 2.3 Characterization

The steps of $O_2$-temperature programmed desorption ($O_2$-TPD) were similar with our previous work,[17] 200 mg of fresh catalyst was loaded, and adsorbed in $O_2$ at 300 $^oC$ for 60 min. After the powder was cooled to 50 $^oC$, it was blown by $N_2$ for 120 min. The catalyst was then heated to 750 $^oC$ at a linear heating rate of 10 $^oC$/min in the $N_2$ flow. The effluent gas was analyzed with a mass spectrometer. The BET surface area and pore volume were measured on a NOVA1000e instrument of Quantachrome Company.[18] To obtain surface textural details of the support, the morphology and structure of the catalysts were studied using a scanning electron microscope (SEM, JEOL/EO, JSM-5900). TEM measurement was performed on the JEOL-JEM-200CX transmission electron microscopy. The Fourier-transform infrared (FTIR) spectra were measured in a TENSOR27 spectrophotometer from Bruker Corporation. Operating parameters were: intervals of 4000-1000 $cm^{-1}$, a 4 $cm^{-1}$ resolution with 32 scans. The measurements were carried out by placing films of the samples mixing with KBr. The measured amount of tested sample was fixed at 10 mg each time. The phase purity of the sample was confirmed by X-ray diffraction (XRD) measurement. It was performed with an MPD type X'pert powder diffractometer equipped with Cu-Kα (λ= 1.54056 Å) radiation, which was operated at 40 kV and 30 mA for 2θ angles ranging from 10$^o$ to 80$^o$. The particle sizes were calculated by Scherrer equation. The XPS spectra were performed on the XSAM 800 spectrometer with an Al anode using Kα (1486.6 eV) radiation. The binding energies in XPS spectra were referenced with respect to the C 1s binding energy of adventitious carbon in the catalysts at 285.1 eV.

### 2.4 CO oxidation

The catalytic performance was evaluated with a fixed-bed flow reactor. 100 mg sample powder was used as catalyst. The reactant consisting of 1% CO and 21% $O_2$ and 78% Ar was fed at a rate of 30 mL/min (18,000mL $h^{-1}$ $g^{-1}$ cat). The composition of the effluent gas was detected with an online SC-200 gas chromatograph equipped with a TDX-01 column. The CO conversion was calculated from the change of CO concentration in the inlet and outlet gases.

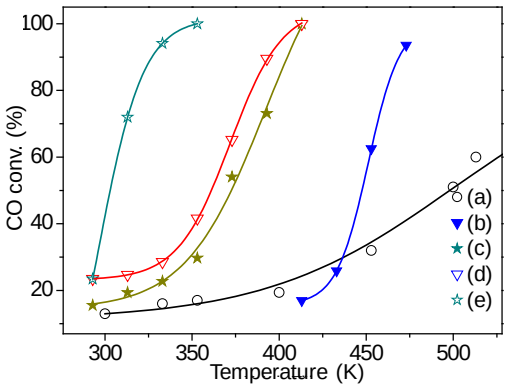


Figure 1. Catalytic performances during CO oxidation: $Au/SiO_2$-C(a), $CoO_x/SiO_2$-C(b), $CoO_x/SiO_2$-PO(c), $Au/CoO_x/SiO_2$-C(d), and $Au/CoO_x/SiO_2$-PO(e); Conditions: 18000 ml/(g·h), V(CO)/ V($O_2$)/ V(Ar) = 1/21/78.

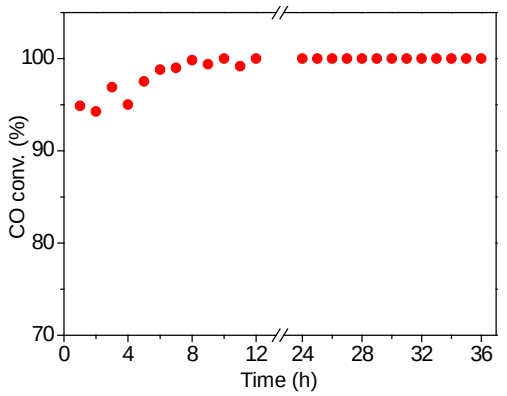


Figure 2. Catalytic performance of $CoO_x/SiO_2$-PO in CO oxidation: Conditions: 330 K, 18000 mL·$h^{-1}$·$g_{cat}^{-1}$, V(CO)/V($O_2$)/V(Ar) = 1/21/78.

## 3 Results and discussion

### 3.1 Catalytic activity and stability for CO oxidation

The low-temperature CO oxidation performances over different gold catalysts are displayed in Figure 1. It can be seen that the $CoO_x$ modified silica possesses the initial activity for CO oxidation. The $CoO_x/SiO_2$-C under conventional calcination shows poor catalytic activity. The light-off



 

temperature (temperature corresponding to 10% CO conversion) under current reaction condition over $CoO_x/SiO_2$-C is only 405 K, and 100% CO conversion is achieved at 478 K. Whilst after plasma treatment under $O_2$ atmosphere, the activity of $CoO_x/SiO_2$-PO for CO oxidation are obviously enhanced, which is lighted off even under room temperature. The temperature related to complete CO oxidation over $CoO_x/SiO_2$-PO are only 410 K.

The CO conversion at room temperature over $Au/CoO_x/SiO_2$-C increases to 24%, and further reaches 100% at 410 K. For the sample after plasma treatment, the higher activities for CO oxidation are achieved over $Au/CoO_x/SiO_2$-PO sample. The CO conversion over the $Au/CoO_x/SiO_2$-PO arrives 40% and 100% at room temperature and 328 K respectively, exposing the great superiority of plasma treatment.

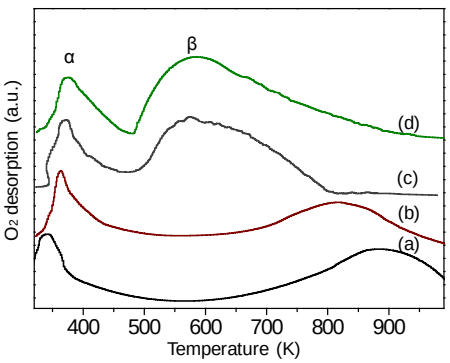


Figure 3. $O_2$-TPD patterns of the typical catalysts: $CoO_x/SiO_2$-C(a), $CoO_x/SiO_2$-PO(b), $Au/CoO_x/SiO_2$-C(c), and $Au/CoO_x/SiO_2$-PO(d).

The long-term performance of $Au/CoO_x/SiO_2$-PO sample for CO oxidation is shown in Figure 2. During the tested 36 h, the CO conversion keeps at 100% after the stable of the catalyst, showing the steady catalytic activity of the $O_2$ plasma treated sample.

### 3.2 Redox properties of catalysts

The activity of catalysts during oxidation reactions largely depends on the oxygen supply ability. The oxygen supply ability lies on the number of oxygen supply center and oxygen active sites.[17] The reversible cycle of releasing and transferring the active oxygen species on the catalyst surface is responsible for the continuous proceeding of reaction. In general, the temperature of oxygen desorption peak reflects the activity of oxygen supply center, and the area of desorption peak is related to the number of oxygen supply center.

It has been reported that the balance of $O_2$ (ads) ↔ $O_2^-$ (ads) ↔ $O^-$ (surf) ↔$O_2^{2-}$ (surf) ↔ $O^{2-}$ (lattice) existed on the surface of catalysts, where the adsorbed oxygen species, $O_2$ (ads) and $O^{2-}$ (ads), were easy to be desorbed under low temperature. However, the $O^{2-}$ (lattice) species could only be desorbed under high temperature.[17] The $O_2$-TPD profiles of four different materials are shown in Figure 3. All the tested samples present two desorption peaks, one at lower temperature (marked as α peak), and another at higher temperature (marked as β peak). The α peak locates around 300-470 K with the peak area generally unchanged (Table 1), indicating the analogous desorption and supplementation ability of surface adsorbed oxygen species ($O_2$, $O_2^-$). The high temperature desorption peak on the contrary, is totally different over the materials before and after gold loading. The related β peaks appear at 885 K and 817 K over $CoO_x/SiO_2$-C and $CoO_x/SiO_2$-PO, respectively.

Table 1 Parameters from $O_2$-TPD results over four typical catalysts.

| Catalyst | Temperature (K) | | Peak area | |
|---|---|---|---|---|
| | α peak | β peak | α peak | β peak |
| $CoO_x/SiO_2$-C | 342 | 885 | 4891 | 8622 |
| $CoO_x/SiO_2$-PO | 363 | 817 | 4649 | 7013 |
| $Au/CoO_x/SiO_2$-C | 373 | 577 | 5343 | 11439 |
| $Au/CoO_x/SiO_2$-PO | 376 | 585 | 4748 | 18589 |

Whilst after gold loading, the corresponding desorption peaks of $Au/CoO_x/SiO_2$-C and $Au/CoO_x/SiO_2$-PO samples are greatly lowered to 577 K and 585 K, respectively. The peak area is also largely increased after gold loading, especially for the gold catalyst treated by plasma under $O_2$ atmosphere, in which the peak area increases about 62.5% comparing to the conventional $Au/CoO_x/SiO_2$-C sample, and 165.1% comparing to the $CoO_x/SiO_2$-PO without gold nanoparticles. That is, the plasma-treated gold catalyst possesses higher amount of oxygen supply center, which give the chance for accelerating the oxygen transformation through solid-gas phases, facilitating the moving of active oxygen species among the lattices, and benefiting the catalytic activity for CO oxidation in turn.

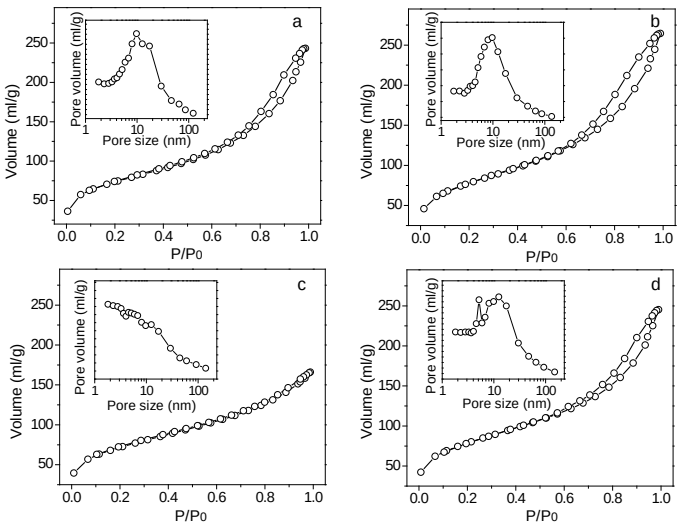


Figure 4. Nitrogen adsorption-desorption isotherms and pore size distribution of two different catalysts: $CoO_x/SiO_2$-C(a), $CoO_x/SiO_2$-PO(b), $Au/CoO_x/SiO_2$-C(c) and $Au/CoO_x/SiO_2$-PO(d).

In addition, it was reported that the highly active oxygen species such as $O^{2-}$, $O^-$, and $O_2^{2-}$ species could be generated when the oxygen went through plasma treatment.[19] The generated oxygen species on the one hand could help to disperse the active sites, and on the other hand reacted with the toxicants to form gaseous production.[19] Under this circumstance, the $O_2$ atmosphere plasma treatment can also help to remove the poisonous compounds such as $Cl^-$ from the

surface of gold catalysts other than the $N_2$ atmosphere, hence protecting the gold nanoparticles from growing into large aggregations.

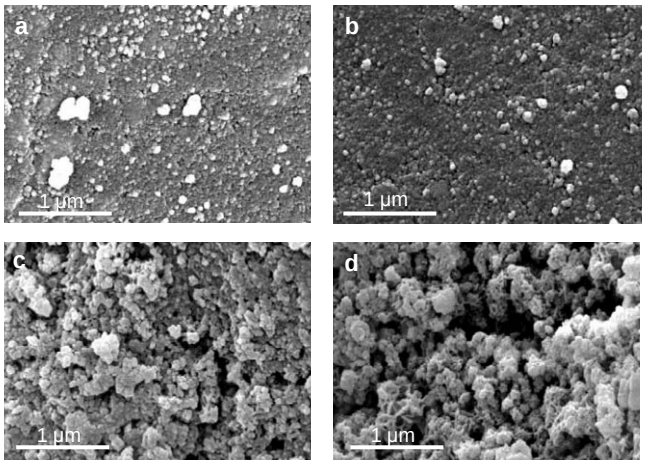


Figure 5. SEM patterns of the typical catalysts: $CoO_x/SiO_2$-C(a), $CoO_x/SiO_2$-PO(b), $Au/CoO_x/SiO_2$-C(c), and $Au/CoO_x/SiO_2$-PO(d).

### 3.3 Morphologies of catalysts

The $N_2$ adsorption-desorption isotherms and pore size distribution of $CoO_x/SiO_2$ samples before and after $O_2$ plasma treatment are illustrated in Figure 4(a-b).

According to the Brunauer classification standard, both of the two supports display the typical Langmuir IV isotherm. In the low pressure region, the adsorption amount rises with the incremental relative pressure; then intensely increases with the further increase of pressure after $P/P_0$ reaching 0.6 due to the capillary condensation.[20] Whilst desorption procedure is irreversible from the adsorption procedure. The rapid desorption process caused the formation of hysteresis loop along with the decrease of relative pressure, indicating the existence of mesopores. The specific surface areas of two samples are calculated from BET equation. The surface area of $CoO_x/SiO_2$-C (251.5 $m^2/g$) is slightly lower than that of the $CoO_x/SiO_2$-PO (265.3 $m^2/g$). The relative pressure corresponding to the shutting of hysteresis loop reflects the mesopores distribution. That is, $N_2$ adsorption-desorption isotherm: the material with narrower size mesopore distribution is going to display larger distance between upper and lower closing points of the hysteresis loop. Directly from the $N_2$ adsorption-desorption isotherms, the $CoO_x/SiO_2$-PO sample under $O_2$ plasma treatment shows more uniform size distribution with average pore size of about 10 nm, whereas the $CoO_x/SiO_2$-C sample displays a broad size distribution with peak maximum around 10 nm and 18.2 nm, respectively.

Despite the decrescent opening of the hysteresis loop, the gold loading does not vary the isotherm obviously as shown in Figure 4(c-d). The two supported gold samples also display typical Langmuir IV type isotherm, indicating that the related materials possess mesoporous structure. Unlike the H2 type of hysteresis loops over $CoO_x/SiO_2$ and $Au/CoO_x/SiO_2$-PO-related to the ink-bottle like pores, the hysteresis loop of $Au/CoO_x/SiO_2$-C is a classical H4 type- corresponding to the uniform and slit-shaped porous structure. However, the surface area of $Au/CoO_x/SiO_2$-PO gently decreases to 252.1 $m^2/g$ comparing with the $CoO_x/SiO_2$-PO (265.3 $m^2/g$), suggesting that the $O_2$ plasma treatment barely changes the porous structure of different samples. On the contrary, the surface area of $Au/CoO_x/SiO_2$-C is reduced to 206.2 $m^2/g$ after gold loading, illustrating the structure of material may transform after gold loading. Besides, a great portion of smaller pores appeared in the $Au/CoO_x/SiO_2$-C with gold loading, which should be caused by the blocking of gold nanoparticles into the mesoporous structure.

The SEM images of four typical samples are shown in Figure 5. The contrast in SEM images (Figure 5a-b) points out the location of $CoO_x$ particles (White spots) and silica (the gray basement). It can be seen obviously that the surface of silica in $CoO_x/SiO_2$-C is covered with heterogeneous $CoO_x$ particles. On the contrary, the more uniform particles can be found on the surface $CoO_x/SiO_2$-PO with plasma treatment under $O_2$ atmosphere. After the gold loading and calcination, the morphology of $Au/CoO_x/SiO_2$-C seems different. The gold species may spread on the surface of support, making the surface to be fluffy. The gold loading procedure may also induce the blocking of mesopores in this sample as revealed by Figure 4a and 4c due to the partial covering of gold particles. However, the $Au/CoO_x/SiO_2$-PO displays a totally different morphology with flocculent morphology and developed porous structure.

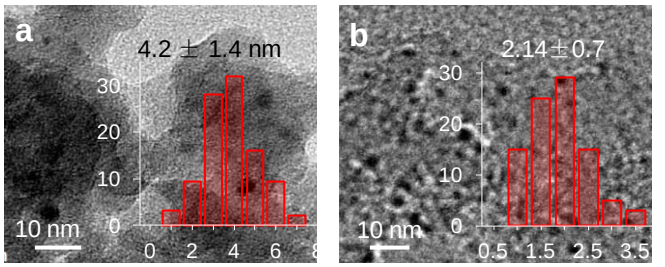


Figure 6. TEM patterns and size distributions of supported gold catalysts: $Au/CoO_x/SiO_2$-C(a) and $Au/CoO_x/SiO_2$-PO(b).

The transmission microscope (TEM) images of supported gold nanoparticles are illustrated in Figure 6. The gold nanoparticles are visualized as black spots. The gold particles of $Au/CoO_x/SiO_2$-C are heterogeneous and around 3-5 nm. The $O_2$ plasma-treated gold nanoparticles in $Au/CoO_x/SiO_2$-PO sample are highly distributed on the surface of support with sizes only around 1-3 nm. As it is mentioned previously, only gold nanoparticles small enough to lose the macroscopic properties could possess efficient activity for CO oxidation.[21, 22] The sizes of supported gold nanoparticles under different treatments all step into nano-scale > 5 nm, which are able to perform reasonable low-temperature CO oxidation activity.

The above results of morphologies of samples under different treatments evidence the efficiency of plasma for modifying the available contact surface, promoting the porosity development,



 

preventing the pores from blocked. These superiorities in turn provide the chance to benefit the reactants adsorption/dissociation and reaction rate acceleration during the CO oxidation.

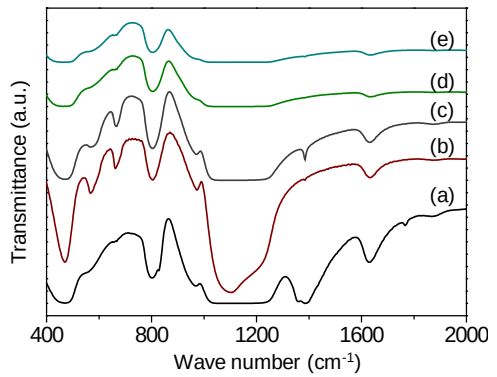


Figure 7. FT-IR patterns of various catalysts: $CoO_x/SiO_2$(a), $CoO_x/SiO_2$-C(b), $CoO_x/SiO_2$-PO(c), $Au/CoO_x/SiO_2$-C(d), and $Au/CoO_x/SiO_2$-PO(e).

### 3.4 Chemical composition and property of catalysts

The characteristics of molecular structures can be reflected by the wavelength and intensity of absorption band in the FT-IR spectrum. Here in this case, the FT-IR spectrum can be applied for identifying the composition and chemical groups in the concerned material. In order to analysis the fine chemical structure of different samples, the FT-IR spectrum are utilized to silica doped with $CoO_x$ before and after special treatment and their supported gold catalysts, as shown in Figure 7. The fresh $CoO_x/SiO_2$ before calcination possesses multiple absorption peaks. The peaks around 460 $cm^{-1}$ and 800 $cm^{-1}$ can be ascribed to the bending vibration of O-Si-O and Si-O-Si, respectively. There is no observation of Si-O-Si stretching vibration that should be around 1100 $cm^{-1}$ due to the covering effect of adjacent absorption peaks. The shoulder peak locates around 946 $cm^{-1}$ is assigned to the non-bonded Si-O- surrounding silica.[22] The symmetric stretching vibration of N=O in the nitrate compound is around 1390 $cm^{-1}$, and the obvious absorption peak at 1640 $cm^{-1}$ should be due to the water species in the samples.

The IR spectra of $CoO_x/SiO_2$-C and $CoO_x/SiO_2$-PO samples display additional absorption peaks at 568 and 667 $cm^{-1}$, corresponding to the stretching vibration of metal-oxygen bond, which is the characteristic absorption peak of $Co_3O_4$ spinel. The former peak around 568 $cm^{-1}$ is resulted from $Co^{2+}$-O vibration.[23] In addition, the N=O stretching vibration (1390 $cm^{-1}$) in the $CoO_x/SiO_2$-C sample disappears, indicating the complete decomposition of nitrate precursor. However, weak absorption peak at 1390 $cm^{-1}$ remains in the $CoO_x/SiO_2$-PO sample treated by plasma. In fact, different from $CoO_x/SiO_2$-C, there is no further calcination of the $CoO_x/SiO_2$-PO after plasma treatment. Unlike the high-temperature calcination that is able to decompose the precursor entirely, the plasma treatment proceeded under gentle condition may keep some residual nitrate species.[11] After the gold loading, the absorption peaks of silica species and $Co_3O_4$ spinel of both $Au/CoO_x/SiO_2$-C and $Au/CoO_x/SiO_2$-PO are weakened. On the other hand, the samples with gold loading display very weak water absorption peak (1640 $cm^{-1}$), suggesting the better water-resistance ability.

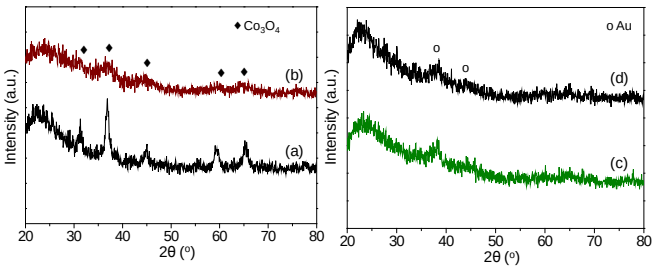


Figure 8. XRD patterns of samples before and after gold loading: $CoO_x/SiO_2$-C(a), and $CoO_x/SiO_2$-PO(b), $Au/CoO_x/SiO_2$-C(c), and $Au/CoO_x/SiO_2$-PO(d).

The XRD spectra of different samples are profiled in Figure 8. The broad diffraction peak appears in all the samples at 22° is ascribed to the amorphous $SiO_2$ phase (JCPDS #27-0605). The diffraction peaks locating around 32°, 36°, 44°, 59°, and 66° in $CoO_x/SiO_2$-C should be corresponding to the surface $Co_3O_4$ species (JCPDS #74-2120). The intensive and sharp diffraction peaks witnesses the existence of large crystallized $CoO_x$ particles. In the plasmas-treated $CoO_x/SiO_2$-PO sample, the $Co_3O_4$ diffraction peaks are largely weakened and broadened, resulting from the high dispersion of $CoO_x$ species in these samples.[7] The dispersed $Co_3O_4$ particles possess the opportunity to expose more active sites, and able to behave better performance for reactions such as CO oxidation.

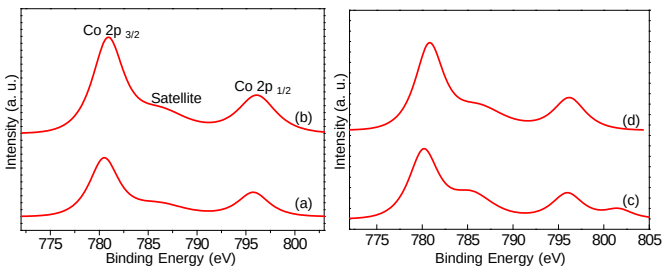


Figure 9. Co *2p* XPS patterns of two typical $CoO_x/SiO_2$ samples: $CoO_x/SiO_2$-C(a) and $CoO_x/SiO_2$-PO(b), $Au/CoO_x/SiO_2$-C(c), and $Au/CoO_x/SiO_2$-PO(d).

The XRD profiles over gold catalysts under different treatments are shown in the right image of Figure 8. It can be seen again that the gold loading do not lead to serious change of the structure. Both the diffraction peaks of amorphous $SiO_2$ around 22° and metallic gold around 38° and 45°Au (JCPDS #65-8601) can be observed from the XRD profiles. None of the samples with gold loading present the peaks of $Co_3O_4$ species, which may be caused by the redispersion of $CoO_x$ species after gold loading.

The Co 2p XPS spectra over several typical samples are displayed in Figure 9. The peaks with binding energy around 781.0 EV and 796.0 eV can be assigned to Co $2p_{3/2}$ and Co $2p_{1/2}$ peaks, with the satellite peak around 786.0 eV. Comparing to the traditional calcined $CoO_x/SiO_2$-C, the binding energy of

$CoO_x/SiO_2$-PO slightly shifts to higher region.[24, 25] Although the $Co^{2+}$ and $Co^{3+}$ possesses the corresponding binding energy around 780.9-781.4 eV and 779.7-779.9 eV,[24] it is still difficult to distinguish the main peak from CoO and $Co_3O_4$ phase due to very narrow distance. Combining with the results from XRD, the Co $2p_{3/2}$ peak with a binding energy around 780.5 eV is inferred as a combination of two overlapped peaks. The corresponding Co *2p* XPS profiles of $Au/CoO_x/SiO_2$-C and $Au/CoO_x/SiO_2$-PO samples are also shown in Figure 9. The binding energy of Co $2p_{3/2}$ around 780.7 eV, suggesting the existance of $Co_3O_4$ spinel in both the catalysts with gold loading.

Table 2 Surface analysis of two typical $CoO_x/SiO_2$ samples from XPS results.

| Catalyst | Surface composition % | | | Intensity ratio |
|---|---|---|---|---|
| | Co | Si | O | Co/Si ($10^{-1}$) |
| $CoOx/SiO_2$-C | 1.88 | 25.92 | 72.20 | 0.73 |
| $CoOx/SiO_2$-PO | 4.11 | 24.82 | 71.07 | 1.66 |

Besides, the $CoO_x/SiO_2$-PO shows larger area peak of Co *2p* than $CoO_x/SiO_2$-C, indicating the higher amounts of $CoO_x$ species on the surface after plasma treatment (Table 2). This result, from another point of view, evidences the fact that plasma treatment facilitates the formation of higher amount of smaller $CoO_x$ particles. After gold loading, the $Co_3O_4$ spinel can be detected in both the $Au/CoO_x/SiO_2$-C and $Au/CoO_x/SiO_2$-PO samples from the XPS spectra (not shown).

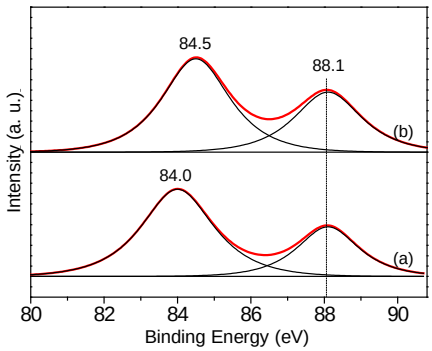


Figure 10. Au *4f* XPS patterns of two typical $Au/CoO_x/SiO_2$ catalysts: $Au/CoO_x/SiO_2$-C(a) and $Au/CoO_x/SiO_2$-PO(b).

The Au 4f spectra of the above two gold catalysts are presented in Figure 10. It was reported by Chen et al.[26] that the binding energy of $4f_{7/2}$ and Au $4f_{5/2}$ of metallic $Au^0$ should be appeared around 84.0 eV and 87.7 eV, respectively. While the peaks around 86.0 eV and 89.6 eV are due to the oxidized gold species ($Au^{3+}$). Directly from Figure 10, it can be seen that $Au^0$ acts as the main gold species in both the catalysts. There is no clear observation of oxidized gold species in the samples, suggesting that there is no such kind of species or only trace amount exists (due to the fact that very few amount of gold species may be reduced during the XPS measurement). Generally speaking, the shifting of binding energy in the supported gold nanoparticles can be related to the sizes of gold nanoparticles. Lim et al.[26] applied STM (scanning tunneling microscopy) and XPS techniques and found out that the binding energy of Au 4f shifted 0.8 eV to higher value along with the decreased particle size. Comparing with $Au/CoO_x/SiO_2$-C, the Au $4f_{7/2}$ binding energy of $Au/CoO_x/SiO_2$-PO raises up about 0.5 eV, which can be viewed as an indication of smaller particle sizes in the plasma-treated $Au/CoO_x/SiO_2$-PO catalysts. This conclusion is in accordance with the results from TEM and XRD.

## Conclusions

In this work, the $CoO_x$ doped silica was used as carrier for gold nanoparticles. The impact of plasma treatment under $O_2$ atmosphere over both the carrier and supported gold nanoparticles were discussed in detail. The $O_2$ plasma-treated sample displayed superior activity and stability for CO oxidation. By analysing the microstructures, morphologies, and the chemical compositions of typical samples, the enhancement of plasma treatment and how it works were exposed in detail. The following conclusions can be obtained.

· The variation of morphologies of plasma-treated samples evidenced the efficiency of plasma treatment on modifying the available contact surface, promoting the porosity development, preventing the pores from blocked.

· Only metallic $Au^0$ species exist in the supported gold catalysts. The gold nanoparticles in the plasma-treated samples are smaller and homogeneous, which are even highly dispersed on the surface of support.

· The $O_2$ plasma treatment is helpful for enhancing the redox properties of materials, which modified the synergy between gold and cobalt particles, and in turn improve the redox properties, and facilitate the supply-supplementary circle of active oxygen species during reaction.

## Acknowledgements

This work was supported by the Natural Science Foundation of China (20776089) and New Century Excellent Talent Project of China (NCET-05-0783).

## Notes and references

[a] *Department of Chemical Engineering, Yibin University, Yibin 644000, Sichuan, China;*
[b] *Department of Chemical Engineering, Sichuan University, Chengdu 610065, China;*
[c] *Institut de Physique et Chimie des Matériaux de Strasbourg (IPCMS), UMR 7504 du CNRS, Université de Strasbourg, 23 rue du Loess, BP 43, 67034, STRASBOURG Cedex 2, France.*
** Corresponding author. E-mail address: chuwei1965scu@163.com (Pr. W. CHU);jluo@ipcms.u-strasbg.fr (Dr. J.J. LUO); Phone numbers: +86 28 85 40 38 36*

## References

1. Q. Wang, X. K. Wang, Z. F. Chai and W. P. Hu, *Chem Soc Rev*, 2013, 42, 8821-8834.
2. V. E. Fortov, A. V. Ivlev, S. A. Khrapak, A. G. Khrapak and G. E. Morfill, *Phys Rep*, 2005, 421, 1-103.

3. N. A. Savastenko, K. Anklam, A. Quade, M. Bruser, A. Schmuhl and V. Bruser, *Energ Environ Sci*, 2011, 4, 3461-3472.
4. S. Mahammadunnisa, P. M. K. Reddy and C. Subrahmanyam, *Rsc Adv*, 2014, 4, 4034-4036.
5. K. H. Yu, Z. H. Wen, H. H. Pu, G. H. Lu, Z. Bo, H. Kim, Y. Y. Qian, E. Andrew, S. Mao and J. H. Chen, *J Mater Chem A*, 2013, 1, 188-193.
6. A. Y. Khodakov, W. Chu and P. Fongarland, *Chem Rev*, 2007, 107, 1692-1744.
7. H. Y. Xu, W. Chu, L. M. Shi, S. Y. Deng and H. Zhang, *React Kinet Catal L*, 2009, 97, 243-247.
8. W. Chu, L. N. Wang, P. A. Chernavskii and A. Y. Khodakov, *Angew Chem Int Edit*, 2008, 47, 5052-5055.
9. D. Van Thanh, L. J. Li, C. W. Chu, P. J. Yen and K. H. Wei, *Rsc Adv*, 2014, 4, 6946-6949.
10. C. J. Liu, K. L. Yu, Y. P. Zhang, X. L. Zhu, F. He and B. Eliasson, *Appl Catal B-Environ*, 2004, 47, 95-100.
11. H. Y. Xu, W. Chu, L. M. Shi, H. Mang and J. Zhou, *Acta Phys-Chim Sin*, 2008, 24, 1085-1089.
12. H. Y. Xu, W. Chu, J. J. Luo and T. Zhang, *Chem Eng J*, 2011, 170, 419-423.
13. H. Y. Xu, W. Chu, J. J. Luo and M. Liu, *Catal Commun*, 2010, 11, 812-815.
14. Y. Azizi, C. Petit and V. Pitchon, *J Catal*, 2010, 269, 26-32.
15. S. Belin, C. L. Bracey, V. Briois, P. R. Ellis, G. J. Hutchings, T. I. Hyde and G. Sankar, *Catal Sci Technol*, 2013, 3, 2944-2957.
16. M. A. Al-Daous, A. A. Manda and H. Hattori, *J Mol Catal a-Chem*, 2012, 363, 512-520.
17. J. J. Luo, H. Y. Xu, Y. F. Liu, W. Chu, C. F. Jiang and X. S. Zhao, *Appl Catal a-Gen*, 2012, 423, 121-129.
18. J. Luo, Y. Liu, W. Sun, C. Jiang, H. Xie and W. Chu, *Fuel*, 2014, 123, 241-247.
19. K. L. Yu, C. J. Liu, Q. Xia, J. J. Zou and B. Eliasson, *Prog Chem*, 2002, 14, 456-461.
20. G. Mistura, A. Pozzato, G. Grenci, L. Bruschi and M. Tormen, *Nat Commun*, 2013, 4.
21. G. C. Bond and D. T. Thompson, *Appl Catal a-Gen*, 2006, 302, 1-4.
22. J. J. Luo, W. Chu, S. Sall and C. Petit, *Colloids and Surfaces A: Physicochemical and Engineering Aspects*, 2013, 425, 83-91.
23. H. Qi, J. Ma and P. Z. Wong, *Colloid Surface A*, 2002, 206, 401-407.
24. C. S. Sharma, R. Awasthi, R. N. Singh and A. S. K. Sinha, *Phys Chem Chem Phys*, 2013, 15, 20333-20344.
25. R. Moreno-Tost, E. R. Castellón and A. Jiménez-López, *Journal of Molecular Catalysis A: Chemical*, 2006, 248, 126-134.
26. C. T. Chang, B. J. Liaw, C. T. Huang and Y. Z. Chen, *Appl Catal a-Gen*, 2007, 332, 216-224.